Modelling amorphous materials via a joint solid-state NMR and X-ray absorption spectroscopy and DFT approach: application to alumina

Angela F. Harper[a], Steffen P. Emge[b], Pieter C. M. Magusin[b,c], Clare P. Grey[b], Andrew J. Morris *[d]

Understanding electronic structure is a crucial component in the development of many functional materials including semiconductors, transparent-conducting oxides, and batteries, and is necessarily directly dependent on their underlying atomistic structure. The elucidation of atomistic structure is impeded, both experimentally and computationally, by structural disorder, presenting a huge challenge for designing functional amorphous materials. Amorphous materials may be characterised through their local atomic arrangements using, for example, solid-state NMR and X-Ray Absorption Spectroscopy (XAS). By using these two spectroscopy methods to inform the sampling of configurations from ab initio molecular dynamics we devise and validate an amorphous model, choosing amorphous alumina to illustrate the approach due to its wide range of technological uses. Our model predicts two distinct geometric arrangements of AlO_5 coordination polyhedra and determines the origin of the pre-edge features in the Al K-edge XAS. We finally construct an average electronic density of states for amorphous alumina, and identify localized states at the conduction band minimum (CBM). We show that the CBM is comprised of Al 3*s* states and connect this localization and the presence of the pre-edge in the XAS. Deconvoluting this XAS by coordination geometry reveals contributions from both AlO_4 and AlO_5 geometries at the CBM give rise to the pre-edge, which provides insight into the role of AlO_5 in the electronic structure of alumina. This work represents an important advance within the field of solid-state amorphous modelling, providing a method for developing amorphous models through comparison of experimental and computationally derived spectra, which may then be used to determine the electronic structure of amorphous materials.

Introduction

Atomistic quantum mechanical modelling has played a critical role in driving many of the advances made involving crystalline materials over the last two decades – originally in terms of rationalizing materials properties, but now increasingly in predicting and optimizing both materials and devices [1–4]. A significant challenge, however, lies in applying the same quantum mechanical methods to amorphous materials[4,5], despite their increasing role in devices; these include dielectric layers in organic electronics, and as protective coatings across a range of materials[6–10]. The challenge lies in capturing both the complexity of the local structure and the heterogeneity and structural variations that occur over a variety of length-scales. Amorphous structures lack the translational and point group symmetries present in crystalline materials, which enable calculations of increasingly large cells. It is also non-trivial to validate such a model against relevant experimental structural data, as symmetry allows structure solution from X-ray diffraction (XRD) experiments, while structure solution of amorphous materials relies on techniques such as Nuclear Magnetic Resonance (NMR) and X-ray Absorption Spectroscopy (XAS) to infer local structure. To understand and ultimately improve the electronic properties of an amorphous material, it is imperative to produce an accurate model of local atomic and electronic structure.

Recent progress in applying machine learning to this problem has enabled models of amorphous single element structures such as silicon, carbon, and phosphorus [4,11–13], as well as progress in some two-element systems including HfO_2 and Li_xSi[3,14]. In these methods, machine learning is applied to describe the atomic level interactions using training sets from first principles energy and force calculations; machine learned models therefore have comparable radial distribution factors, bond-lengths, and structure factors to first principles models with improved simulation time and length scales[3]. However, their ability to predict spectral properties such as NMR and XAS with first principles accuracy is lacking; although ShiftML predicts NMR shifts for molecular solids, its nuclei are limited to C, H, N, O, and S[15]. Similarly, XAS spectral lines for transition metal oxides are predicted using a random forest method but applied only to a set of known, crystalline, transition metal oxides[16]. Clearly, there is a need for spectral predictions with first principles accuracy, which can be applied to amorphous materials.

Atomic layer deposited (ALD) alumina is one of the most widely used amorphous coating materials, as it is a model ALD system with well-understood surface chemistry[17,18]. ALD alumina was first employed as a high-*k* dielectric and is present in applications across a range of electronic devices from solar cells to battery electrodes and field-effect transistors. Amorphous alumina (a-Al_2O_3) is a wide band-gap insulator which enables surface passivation, interface stability, and protects against degradation as a coating material[6–8,19,20]. These properties have increased the capacity retention of Li-ion battery electrodes[19–21], enhanced the lifetime of perovskite solar cells[6,22], and improved the catalytic capabilities of metal-organic frameworks[23,24]. Given its clear widespread

[a] *Theory of Condensed Matter, Cavendish Laboratory, University of Cambridge, J. J. Thomson Avenue, Cambridge CB3 0HE, U.K.*
[b] *Yusuf Hamied Department of Chemistry, University of Cambridge, Lensfield Road, Cambridge CB2 1EW, U.K.*
[c] *Institute for Life Sciences & Chemistry, Hogeschool Utrecht, Heidelberglaan 7, 3584 CS Utrecht, Netherlands*
[d] *School of Metallurgy and Materials, University of Birmingham, Edgbaston, Birmingham B15 2TT, U.K.*
† Corresponding Author: a.j.morris.1@bham.ac.uk

applications, an atomic level model of a-Al_2O_3 would be indispensable to the device physics community.

This work presents a method for modelling the local structure of an amorphous material at the quantum mechanical level of accuracy, that is one which describes the electronic structure of an amorphous solid using *first principles* methods, which is then applied to a-Al_2O_3. This method utilizes both *first principles* calculations and high-quality spectroscopy to confirm the detailed electronic structure of a-Al_2O_3. The novelty of our approach lies in the integration of locally sensitive experimental techniques with spectroscopy calculated from first principles We obtain NMR spectra at fields up to 1 GHz, which is the current state-of-the-art in solid state NMR and show that our DFT-based model contains the same structural features captured by these experimental measurements. The atomic level accuracy of this model enables us to identify two distinct five-fold coordination geometries present in a-Al_2O_3, and the orbital character of electronic states at the Al pre-edge of the absorption spectrum, which are unique to a-Al_2O_3. We calculate an average electronic density of states on our model, in a computationally efficient and accurate manner, thereby opening the door for further investigation into amorphous electronic structure.

Methods

Experimental methods

Substrates for ALD were washed with Acetone, Methanol/Ethanol, then deionized water and blow dried with N_2 before deposition. Depositions were performed with a Picosun R-200 Advanced ALD tool attached to an MBraun glovebox. At a chamber base pressure of approx. 12 hPa the substrates were heated to 150°C. Trimethylaluminum (TMAl, EpiValence Ltd, Electronic grade) was used as precursor gas, DI water as reactant and N_2 as purging gas. For each cycle, corresponding to one layer, the substrates were first exposed to precursor gas (flow = 150 sccm), purged, then reactant gas (flow = 200 sccm) and finally the chamber was purged again which completes a cycle. Pulse and purge durations were 0.1 s and 10 s, respectively.

For synchrotron measurements, Al_2O_3 ALD films were deposited on pre-cut 3 mm x 3 mm Si substrates (Pi-KEM, Prime Grade, intrinsic dopant). The substrates originated from a diced 2 inch diameter Si(100) wafer (275±25 µm thick, >200 $\boldsymbol{\Omega}$ ·cm) single-side polished with a thermal dry oxide layer of 20nm±10 percent on both sides. Substrates with varying numbers of ALD layers were prepared, ranging from 2 to 1000. XAS measurements shown in this work were obtained from the 1000 layer sample. For NMR measurements more sample were required, so an 8 inch Si wafer (Picosun) was used and 1000 ALD layers were deposited. Al K-edge XAS total electron yield experiments were conducted at the I09 beamline at Diamond Light source (United Kingdom) in a total electron yield setup.

For NMR spectroscopy measurements, these were taken at three different fields 16.4 T, 11.8 T, and 23.5 T as outlined below. 16.4 T & 11.8 T: ^{27}Al NMR spectra were acquired using Bruker 4 mm HXY MAS probes. 1D spectra were acquired using a regular one-pulse pulse program with a small flip angle ($\pi/6$) on Bruker 700 MHz (16.4 T) and 500 MHz (11.8 T) magnets with Avance III consoles. Two-dimensional ^{27}Al 3QMAS (triple quantum MAS) NMR spectra were acquired on a Bruker 700 MHz (16.4 T) magnet. Quadrupolar pulse optimization was performed on γ-Al_2O_3 powder (Acros Organics). 23.5 T: ^{27}Al NMR spectra were acquired using a Bruker 1.9 mm HXY MAS probe. Spectra were acquired using a rotor-synchronised (40 kHz ≙ 2τ = 50µs) Hahn-echo spectrum with $p2 = 2 \cdot p1 = 5\mu s$ ($\pi/2$= 2.5 µs) on a Bruker 1.0 GHz (23.5 T) magnet with an Avance Neo console. The MAS NMR experiments were performed at sample spinning speeds of 14 kHz (16.4 T & 11.8 T) or 40 kHz (23.5 T). The spectra were externally referenced against AlF_3 powder (-17 ppm [25]) The NMR sample was obtained by scratching off the top layer deposited on the 8 inch wafer using a Wolfram carbide pen. The powder was packed into a 4 mm (16.4 T & 11.8 T) or 1.9 mm (23.5 T) ZrO_2 rotor.

Bruker Topspin software was used for raw data handling and processing. The ^{27}Al spectra were fitted with DMFIT software[26] to obtain integrated ratios and values of average δ_{iso}, average C_Q and ΔCS using the *CzSimple* model with d=5 for the Gaussian Isotropic Model (GIM) case. The best fit is obtained using the GIM case of the Czjzek model[27], corresponding to a distribution of local environments that lead to a spread of quadrupolar coupling constants and chemical shifts.

First-principles spectroscopy

Details of the methods used to generate the amorphous model are given in the following section, **Amorphous model generation**. All AIMD simulations were performed using VASP v5.4.1[28] in the NVT ensemble using a Nose-Hoover thermostat [29] with a plane-wave energy cutoff of 520 eV using projector-augmented wave pseudopotentials [30], and k-point sampling done only at the Γ point. The specific pseudopotentials, parameters, and methods used to calculate the spectroscopy from first principles are described in this section.

Both the XAS and NMR spectra were calculated on each configuration in the model independently and the outputs were summed across configurations to calculate the total spectrum. All spectral calculations, and electronic density of states were calculated at a plane-wave energy cut-off of 1000 eV and a single k-point at Γ in CASTEP v19.11[31]. The CASTEP gauge-including projector augmented wave (GIPAW) method was used to calculate all NMR parameters [31,32], at the PBE functional level of theory using the on-the-fly generated C18 library of pseudopotentials. The NMR parameters were averaged over 45 configurations from *ab* initio molecular dynamics (AIMD) with 48 Al atoms in each cell totalling 2160 ^{27}Al NMR chemical shielding parameters for the a-Al_2O_3 model.

Quadrupolar effects to the NMR spectra were introduced using SIMPSON [33] to carry out spin-simulations at the same sample spinning speeds as the MAS NMR experiments of 14 kHz (16.4 T & 11.8 T) and 40 kHz (23.5 T). The quadrupolar coupling

constants, isotropic shieldings and asymmetry parameters for each Al site were used from the output of the GIPAW NMR calculations. These spectra were obtained without including any broadening in the frequency spectrum and were subsequently broadened using a Gaussian broadening scheme to produce the spectra shown in Fig. 3. To calculate the 2D isotropic vs. quadrupolar shift, the central transition of the quadrupolar shift for MQMAS spectra was calculated as follows,

$$\sigma_{qs}\,(^{27}Al) \;=\; -\frac{3\times 10^4}{5}\times\frac{C_Q^2}{\nu_0^2}(1+\eta_Q^2/3)$$

where ν_0 is the spectrometer frequency in MHz, and η_Q is the asymmetry parameter of the electric field gradient. Both C_Q and η_Q were obtained from DFT calculations of the magnetic shielding parameters. A spectrometer frequency of 182.4 MHz for 27Al, corresponding to a 1H Larmor frequency of 700 MHz, was used for ν_0 .

First principles XAS calculations were carried out by specifying a single atom at which to calculate the absorption edges. One Al atom from each of the 45 configurations was selected at random, in order to obtain a set of atoms on which to calculate the spectra, such that the total 45 Al atoms were in coordination environments which were representative of the 50%, 38%, and 12% of Al(IV,V,VI) environments present in experiment. For each configuration an XAS spectra was calculated using the core-hole pseudopotential method within CASTEP v19.11 [31,34]. To calculate the XAS for the Al K-edge, a pseudopotential with a 1s core-hole was placed on the randomly selected atom within the configuration and charged balanced by placing a total positive charge of +1 on the cell. The absorption spectra was calculated at a plane-wave energy cut-off of 1000 eV, using the HARD pseudopotential library in CASTEP v19.11[35]. The absorption spectrum was produced by OptaDOS v2.1 and broadened using the adaptive broadening scheme[36–38]. This spectrum was referenced using the method of Mizoguchi et al.[39] such that the transition energy is referenced to the difference in energy between the ground state configuration of a-Al_2O_3 and the configuration which includes the core-hole pseudopotential.

Results

Amorphous model generation

Building an amorphous model typically involves a tradeoff between large supercells and classically described inter-atomic potentials, or small cell sizes at a quantum mechanical level of theory, and a limited description of the structure. Intuitively, a high-accuracy inter-atomic potential, large cell size model is the goal, however first principles quantum mechanical calculations using density-functional theory (DFT) scale as $O(N^3)$ making these large cell size accurate calculations unfeasible. Previous models of amorphous alumina from first principles are on the order of 50 to 200 atoms, and any of observables such as electronic DOS or chemical shift consider only a single unit cell[40–42]. Furthermore, these models typically compare to previous experimental work on amorphous alumina, rather than ensuring that the experimental conditions they are comparing to are consistent; given the known interdependence between structure and deposition conditions, especially in the case of amorphous alumina, a direct comparison is imperative, as we will show herein[43].

Our method, outlined in Fig. 1, uses experimentally driven *directed sampling* across a set of high-quality small cell size calculations from *ab initio* molecular dynamics (AIMD) to construct a model which reproduces experimentally known spectroscopic signatures, specific to ALD deposited a-Al_2O_3. The resultant model is a set of static configurations from AIMD which contains local orderings that are representative of the amorphous solid.

To build this model, we first generate a large set of AIMD simulations using a melt-quench technique which span a range of initial conditions (densities, equilibration temperatures, and rate of equilibration) as outlined in Fig. 1 *Structure Generation*. For each set of initial conditions, the AIMD simulations are repeated from different starting structures, thereby exploring additional local structural orderings. From these simulations, the static configurations from the final equilibrated 1000 timesteps of each simulation are considered. For the a-Al_2O_3 model, we generated 18 initial conditions, with 3 starting structures of 120 atoms each to generate a total of 54,000 static configurations. We simulated a-Al_2O_3 at densities of 3.18, 3.30, and 3.42 g/cm^3, equilibration temperatures or 300, 600, and 900 K, and using rates of equilibration which we refer to as a 'cooling' and 'quenching' scheme (the combination of these parameters resulting in 18 distinct initial conditions).

Each of these sets of initial conditions was specifically chosen based on literature of a-Al_2O_3 modelling to narrow the initial input size for our models. The range of densities 3.18, 3.30, and 3.42 g/cm^3 was chosen based on previous experimental literature on a-Al_2O_3 which suggests a range of possible densities between 3.05 to 3.40 g/cm^3 [41,44] and further evidence that a density of 2.9 g/cm^3 is well below what is expected experimentally as this model from Lizarraga *et al.* contained AlO_3 environments which are not observed in experiment[45]. A 120-atom model was used in order allow for computational efficiency, given the computational intensity of both NMR and XAS in DFT. Finally, the 'quenching' and 'cooling' schemes are in line with two distinct methods of amorphous model generation found in the literature[41,46] . Although the cooling method is more commonly employed[41,45], as slower cooling rates have shown to give better results in line with experiment, the 'quenching' method used on a slab model of Al_2O_3 and Al showed consistent radial distribution functions to experiment, prompting us to explore this method.

In both equilibration schemes, 120 atoms with concentration Al_2O_3 were packed into a cubic box, using Packmol [47]. The cell was then melted at a temperature of 4000K for 10 ps (5000 AIMD steps with a 2 fs time step). In the cooling scheme, the cell was then cooled to the desired equilibration temperature using the Nose-Hoover thermostat, whereas in the quenching scheme, the cell was immediately equilibrated from the melt for a further 10 ps. In this *Structure Generation* we have thus captured both the ergodicity across the range of

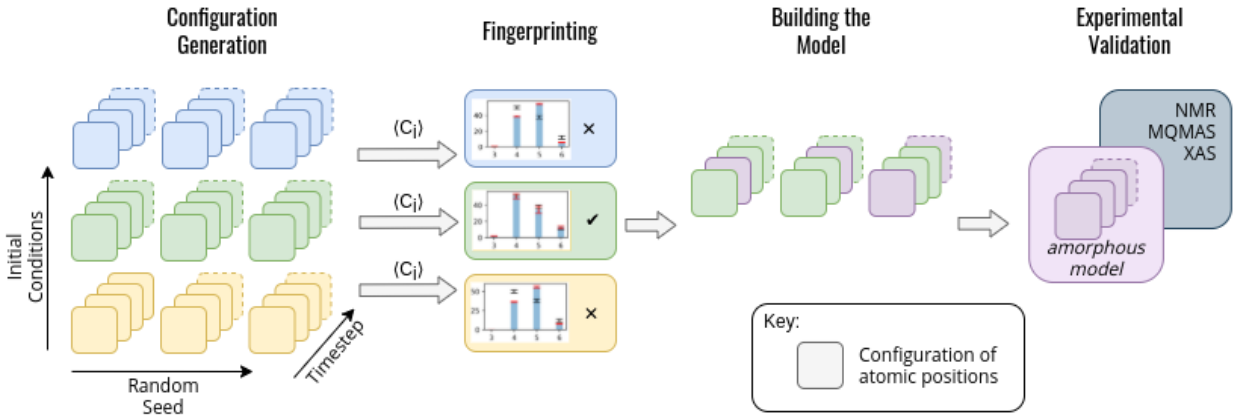

1 Method for generating an amorphous model from a series of static configurations from AIMD. Structure Generation: Each colored box represents a single static configuration from an AIMD simulation, and their depth into the page shows the number of configurations over time (timestep arrow). These configurations are colored by their initial conditions (temperature, density, and rate of equilibration) such that blue, green, and yellow are three different sets of initial conditions. The three repeated sets of configurations represent repeated AIMD simulations with different randomly seeded starting points. In this schematic example there are 3 initial conditions and 3 randomly seeded AIMD simulations for each set of initial conditions. **Fingerprinting**: The results of simulations for each set of initial conditions are averaged across the final equilibrated 1000 AIMD steps of the simulation, and the ratios of coordination environments are compared between the simulation and experiment. Average over configurations which match experimental data are then used for **Building the Model**. The model consists of a total of 45 randomly selected configurations (15 from each individual AIMD simulation out of the 3 randomly seeded AIMD simulations). This model is collated and shown as the purple squares labeled 'amorphous model'. These 45 configurations are then used in the **Experimental Validation** in which the total observable is calculated as an average over static configurations in the amorphous model.

timesteps, and the randomness across the range of AIMD simulations for a-Al_2O_3.

A comparison across all 54 simulations from AIMD of the radial distribution functions (RDF) for a-Al_2O_3 compared to the Lamparter *et al* RDF from 1997[48]is shown in the Supplementary Information Fig. S3. Interestingly, a majority of the models with varying densities, equilibration temperatures, and cooling schemes have comparable RDFs with experiment, prompting a further narrowing of this initial set of data in order to obtain a model which is specific to the experimental ALD deposited a-Al_2O_3 .

In order to select a model which contains similar local structural information to the ALD deposited alumina, we further curate our set of 54 independent simulations from 18 different initial initial conditions using experimental information from NMR in a process known as *Fingerprinting* (Fig. 1). Each set of simulations at a given initial condition is averaged across the 3 AIMD simulations for that set of initial conditions (a total of 3000 static configurations for each set of initial conditions). From this data, the concentrations of Al coordination environments, four- five- and six-fold Al, are extracted and compared to experimental values of 50%, 38%, and 12% ± 2% concentration, respectively (Fig. S1, Fig. S2). These experimental coordination environment concentrations are extracted by fitting the 27Al NMR using the Czjzek model as described in the **Experimental methods** section. All sets of initial conditions that do not meet the tolerances of the experimental concentrations are then excluded, in order to determine the set of initial conditions which will capture the specific local properties of a-Al_2O_3; this is our way of using more informative experimental information to narrow down the configuration space to those simulations that are most likely to capture experimental properties.

Of the 18 initial conditions considered, the *fingerprinting* step identifies two initial conditions which produce models with ratios of four-, five-, and six-fold Al coordination environments within error of the experimental data. These are the set of simulations run at 600K and 300K using the cooling scheme at a density of 3.18 g/cm^3. The results for the 300K model are shown throughout the main text and the 600K results are shown in the Supporting Information with comparable resulting spectra from first principles. The other 16 models, while also within the initial range of possible experimental conditions, therefore likely do not compare to our specific ALD coating of 1000 layers of a-Al_2O_3, but could possibly be used in future work to model other phases of a-Al_2O_3 with varying coordination environments.

Finally, we can construct the amorphous model from the simulations with initial conditions which met the *Fingerprinting* criteria, as a set of randomly selected static configurations. For each initial condition, a set of 15 configurations across the final 1000 timesteps are randomly chosen from each of the 3 AIMD simulations, to create a total of 45 static configurations which make up the *amorphous model*. This is a total of 120 atoms per cell x 45 configurations or 5400 atoms in the amorphous model distributed across smaller cells of 120 atoms from AIMD. In this step, a check was added to ensure that the 45 randomly selected configurations retained the same coordination environment ratios as the original *fingerprinting* step. These 45 configurations are combined and referred throughout as the amorphous model.

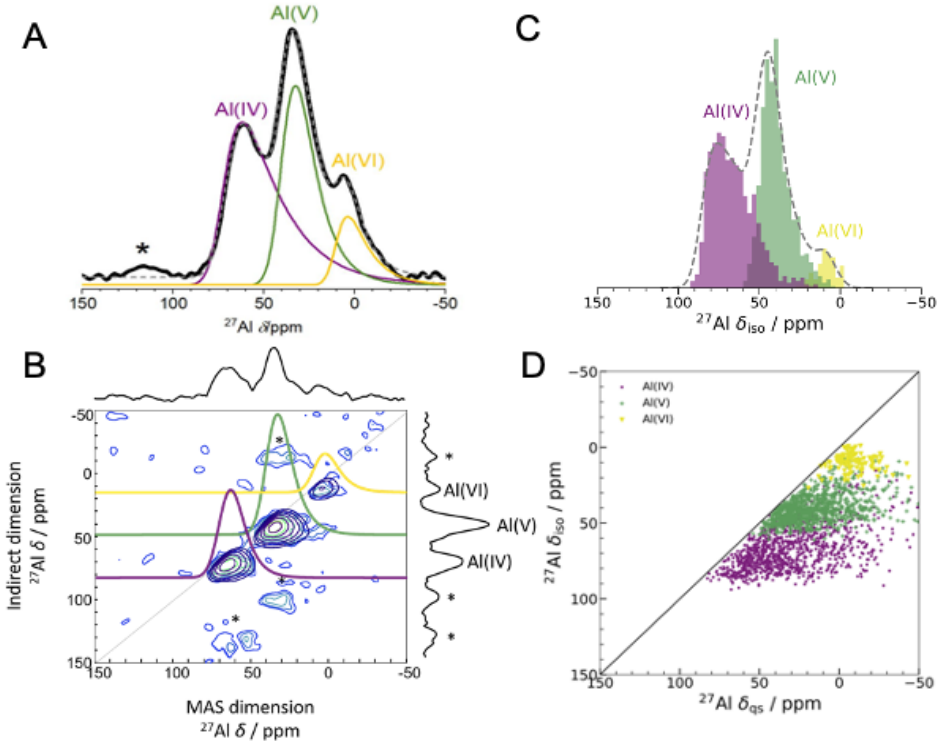

2 Experimental 1D NMR and MQMAS compared to isotropic shieldings from computed NMR from DFT. (A) 1D 27Al experimental NMR (black) at 16.44 T with three fits using the Czjzek model (solid lines; GIM case (see Experimental Methods and Table S 3 for fitting parameters) a model commonly applied to spectra of quadrupolar nuclei such as ^{27}Al when the materials are disordered [27]. The fits are summed to produce overall 1D spectra (dashed grey) of ALD deposited Al_2O_3. Spinning sidebands are indicated with an asterisk. Each signal is colored according to the closest geometric environment, based on experimental shift values for Al(IV,V,VI). **(B)** MQMAS at 16.44 T of ALD deposited Al_2O_3 shows that Al(IV) and Al(V) both have large quadrupolar shifts in the MAS dimension. **(C)** GIPAW NMR calculated spectra of the amorphous model. The distributions of Al environments are shown and broadening of 8 ppm is applied to the total NMR spectrum. Note that this x-axis is δ_{iso} indicating that this is a plot of the isotropic shifts from each individual Al atom, rather than the quadrupolar lineshapes (shown in Fig. 3). This corresponds to the spectrum at an infinitely high magnetic field. **(D)** Comparison of δ_{iso} and δ_{qs} from GIPAW NMR where the second-order quadrupolar shift (δ_{qs}) is calculated using the method from [60]. This method again shows distortions in the quadrupolar dimension for both Al(IV) and Al(V), which is consistent with the MQMAS in **B**. The distribution of δ_{qs} indicates that quadrupolar effects play a large role in the experimental 1D lineshape.

First-principles spectroscopy on a-Al_2O_3

For some desired property, X, such as electronic density of states, we can calculate the average value of this property across these 45 static configurations (N_c) as,

$$X(N) = \sum_{c=1}^{45} X(N_c)$$

This is analogous to an ensemble average of the property in which the probability of each configuration is equally likely, as we are in an amorphous solid with no symmetry equivalence. Herein we show that this amorphous model not only captures global properties such as coordination number, but also the specific local electronic properties predicted by experimental spectroscopy.

By calculating the ensemble average across configurations using the method outlined above, the average NMR and XAS spectra were calculated, and compared to experimental spectroscopy on a 1000 layer sample of ALD deposited a-Al_2O_3. Reproducing these experimental signatures indicates that this model captures the local order, and electronic properties of the experimental amorphous phase.

The experimental ^{27}Al 1D NMR spectrum shown in Fig. 2A shows 3 distinct peaks corresponding to disordered four-, five-, and six-fold coordinated (Al(IV), Al(V) and Al(VI)) Al environments with a ratio of 50%, 38%, and 12% ± 2% respectively. The presence of the Al(V) signal at 40 ppm and the low intensity of the Al(VI) signal at 11 ppm are strong indicators of the amorphous nature[49,50]. It is expected that a distribution of asymmetric Al environments, combined with the quadrupolar nature of the ^{27}Al nucleus ($I = 5/2$), would lead to large quadrupolar coupling constants (C_Q) and a wide range of isotropic chemical shifts, as evidenced by the broad peaks shown in the 1D NMR spectrum in Fig. 2A. The 2D MQMAS (multi quantum MAS) NMR shows three signals spreading along the isotropic diagonal line and horizontally along the MAS dimension, highlighting the spread of quadrupolar coupling constants and a chemical shift distribution (Fig. 2B).

The NMR isotropic shieldings for all 2160 atoms in the amorphous model are calculated using DFT GIPAW NMR and reproduce the total isotropic range and location of shifts in the

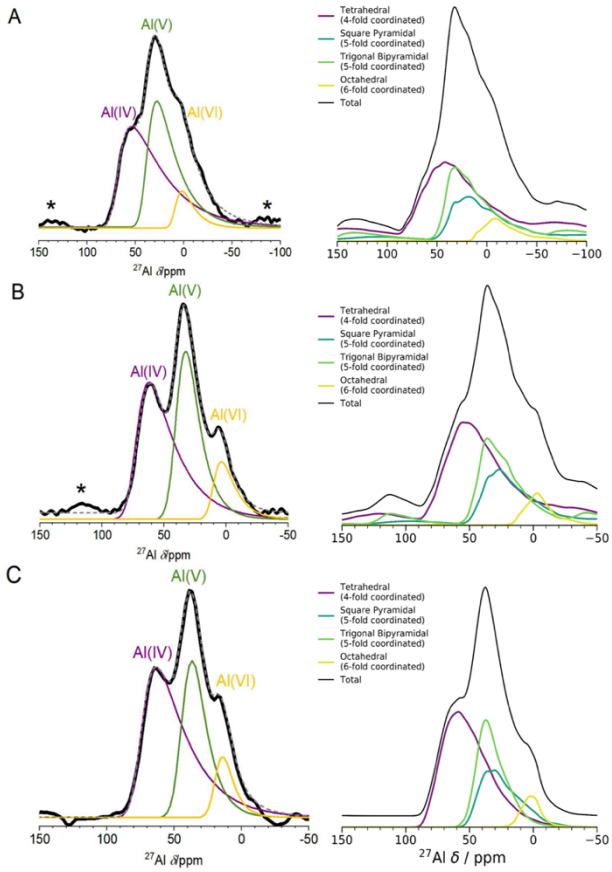

3 **1D ^{27}Al NMR at 3 fields (A 11.75 T, B 16.44 T, C 23.49 T) experimental and computed spectra.** Left panel is experimental spectra, the right panel is calculated spectra with quadrupolar effects calculated using SIMPSON [33]. Two lower field spectra were measured using a one pulse sequence, and the high field spectrum was measured using a Hahn-echo pulse sequence. Spinning sidebands are marked with asterisks in the experimental spectra. Experimental fitting was obtained using a Czejek model. DFT-calculated spectra show Al(V) lineshapes separated into square pyramidal and trigonal bipyramidal environments. These calculated spectra represent the first known DFT-calculated NMR lineshapes of amorphous materials and show excellent comparison to the experimental spectra. At higher fields in both cases the three peaks (Al(IV,V,VI)) become more pronounced, and are easily identifiable as separate environments.

experimental 1D spectrum (Fig. 2C). A wide distribution of C_Q values and calculated quadrupolar induced shifts (δ_{C_Q}) across Al sites which ranges from 10 to 20 MHz (Fig. 2D), with a wider range for both Al(IV) and Al(V) environments. The calculated isotropic shieldings and corresponding quadrupolar shifts show similar trends to experiment, indicating that the model captures these features from NMR. The spin-simulation tool SIMPSON[33] was used to incorporate quadrupolar interactions at three fields (11.75 T, 16.44 T, 23.49 T) corresponding to the three fields at which the experimental NMR spectra (Fig. 3A) were obtained. The resulting spectra are shown in Fig. 3B and the quadrupolar nature of the Al(IV) and Al(V) environments is well described as evidenced by the sloping tails towards lower δ_{iso} values, which are indicators of quadrupolar environments. Furthermore, trends at increasing field strengths are captured by both theory and experiment, with higher fields showing sharper peaks of the Al(IV,V,VI) environments, and a narrower overall spectral width.

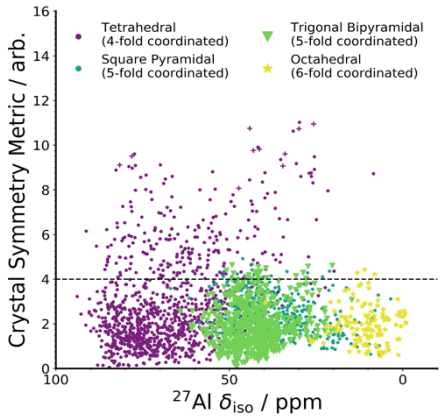

4 **DFT calculated isotropic shielding compared to the distortion of its geometric environment.** GIPAW NMR calculated δ_{iso} versus CSM as defined by ChemEnv [51]. Each coordination environment is broken down into its closest geometric environment and coordination number: Al(IV) sites were classified as tetrahedral, Al(V) sites were subdivided into trigonal bipyramidal and square pyramidal and Al(VI) as octahedral. There are a large number of distorted (CSM > 4) tetrahedral environments, which have a range of δ_{iso} shifts.

One advantage of calculating the NMR spectrum from first principles, is that the calculations retain an individual spectrum for each atom in the model. In this way, we can construct spectra based on atom-specific coordination environments. Using a crystal-symmetry metric (CSM) [51], a measure of the relative distortion from perfect symmetry was extracted for each site in the model. A comparison of the CSM to isotropic chemical shift (Fig. 4), shows that the majority of tetrahedral sites are distorted (CSM > 4)[51] , which agrees with the wide quadrupolar distribution of Al(IV) shifts in experimental MQMAS. Separating the spectra into the closest geometric environment, as shown in Fig. 3, determines that within the a-Al_2O_3, there exist two types of Al(V) environments, square pyramidal and trigonal bipyramidal; these sites combine to make the Al(V) peak in the 1D NMR at 40 ppm, with a range of site-specific shifts from 20 to 60 ppm. Given Al(V)s unique appearance in amorphous Al_2O_3 phases, this identification of two geometries of Al(V) sites suggests that further work should involve identifying the role of each geometry in electronic devices. The first principles model of a-Al_2O_3 enables the construction of these two sites' spectra, where experimental NMR shows them as overlapping.

NMR is a method available for validating the local *atomic* structure while XAS is a measurement for probing the local *electronic* structure of a-Al_2O_3. The Al K-edge XAS spectrum shown in Fig. 5, exhibits three main features; a pre-edge feature (a) and two dominant broad peaks at 1565 eV (b) and 1570 eV (c) which are similar to those in Al-rich glasses [52] and attributed to transitions in Al(IV) and Al(VI) respectively. The absorption edge for Al(V) lies between Al(IV) and Al(VI), and has no experimental reference. Calculating core-hole spectra for all Al sites in the amorphous model, determines the location of this Al(V) absorption edge between 1565 and 1570 eV (Fig. 5), and confirms the absorption energy of the Al(IV) and Al(VI) peaks, implying that the model's electronic structure is consistent with the experimental a-Al_2O_3.

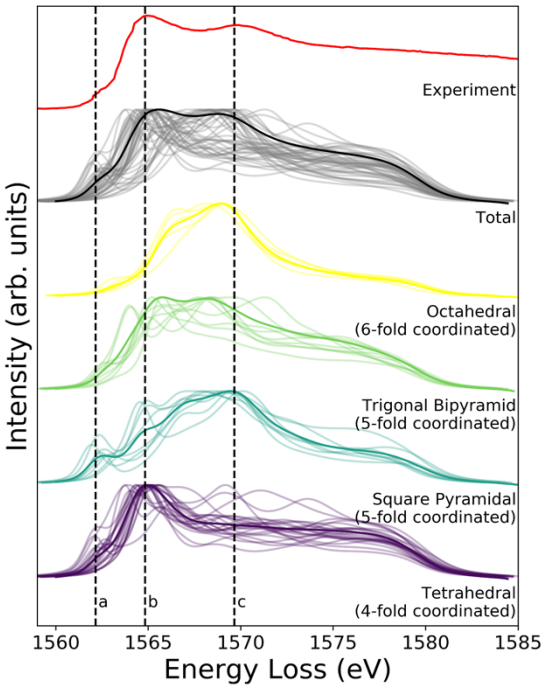

5 **Experimental XAS spectra obtained from the ALD deposited sample compared to the calculated core-hole XAS.** The experimental spectra is identified by the red line labeled Experiment, and is obtained from the 1000 layer ALD deposited sample. Three distinct features at 1562, 1565, and 1570 eV are denoted by dashed lines a, b, and c. The grey lines in the Total spectra show each individual spectra calculated at a single Al site in each configuration from the model, and the solid black line is the sum of those spectra. DFT calculated spectra separated by coordination environment are shown in the bottom four spectra; thin lines are individual spectrum, thick lines are the sum of each geometric site's spectra. All Al(IV) sites were classified as tetrahedral, Al(V) sites were subdivided into trigonal bipyramidal and square pyramidal, and Al(VI) as octahedral. Dashed vertical lines indicate relevant peaks in the experimental spectra.

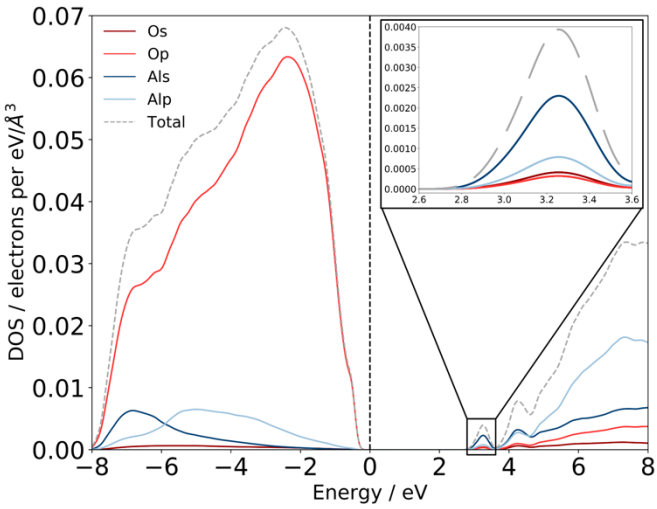

6 **Computed electronic density of states for amorphous alumina.** Total electronic density of states separated by atom and orbital contribution shows that a-Al_2O_3 is a wide bandgap insulator, with a PBE calculated gap of 2.6 eV. States at the top of the valence band, near the fermi level are primarily O *p* states, with states in the conduction band minimum being primarily Al *s* (detail shown inset top right). The dashed grey line is the sum of these states, and the total density of states was broadened using a Gaussian broadening scheme of width 0.1 eV, as implemented in OptaDOS [36,37]. The Fermi level is set to 0 eV for all configurations. Two localized states at 3.2 and 4.2 eV above the Fermi level have Al *s* character and mixed Al *s,p* character, respectively.

In addition to identifying the two main XAS peaks, the pre-peak at 1563 eV was also reproduced. A pre-edge is documented for α-Al_2O_3, at 1565 eV, which occurs because of transitions from the *1s* to *3s* states in Al [53]. While this transition is normally dipole forbidden, the presence of atomic vibrations results in distorted octahedral environments and bond lengthening which causes *p-s* mixing to occur and allow this transition. The pre-edge in a-Al_2O_3 is at 1562 to 1563 eV, both in experiment and in the calculated spectra, as shown in Fig. 5, and occurs in either tetrahedral Al(IV) sites or square pyramidal Al(V) sites. Similarly to the α-Al_2O_3 case, this pre edge is a result of site distortions at the Al(IV) site (Fig. S10)[53]. The calculated XAS spectra suggests a possible origin of this pre-edge feature, arising from Al(IV) sites as well as the absorption energy of the Al(V) peaks, which are masked in experiment, as their absorption energies overlap with transitions in Al(IV) environments.

The method of averaging observable properties across configurations can further be extended to a first-principles specific technique, the electronic density of states (eDOS). The a-Al_2O_3 eDOS is of particular interest, as this material is a coating layer in many electronic devices such as Li-ion batteries, semiconductors, and field-effect transistors. The eDOS, calculated as an average across the 45 configurations in the amorphous model (Fig. 6), confirms the experimentally predicted wide band gap insulating nature of this material. States at the valence band maximum (VBM) are O *p* type character, and states at the conduction band minimum (CBM) are Al *s* character. Interestingly, we identify two small peaks at the bottom of the conduction band at 3.2 and 4.2 eV which are low density, but highly localized states in this material.

Previous experimental XAS on the Al $L_{2,3}$- edge[54] propose that the location of the CBM is governed by the charge transfer from Al to O atoms, specifically between the O 2*p* states at the VBM and Al 3*s* states at the CBM. The eDOS shown in Fig. 5 confirms these experimental assignments of the orbital character and is consistent across each of the 45 configurations in the a-Al_2O_3 model. Further, as Fig. 5 indicates, these localized states at the CBM, which appear as the pre-edge in the XAS, arise from both Al(IV) and Al(V) coordination geometries. The pre-edge feature in both coordination geometries is present at 1562 eV, making it impossible to distinguish the individual contribution from either of the two geometries experimentally. The ability to deconvolute the spectral features arising form either Al(IV) or Al(V) contributions is therefore a unique feature of calculating the XAS from first principles. While such deconvolution is routinely applied in crystalline systems[55–58], this result demonstrates the capability of performing a similar analysis using a joint NMR and XAS analysis on an amorphous material, and determining the orbital character of these states using first principles calculations of the eDOS.

Conclusions

Previous work[3,59] implies that amorphous models require thousands of atoms in the unit cell or semi-infinite simulation times to fully capture local properties. We show that by averaging across AIMD simulations and incorporating experimental insight into the sampling approach, we produce a model of a-Al_2O_3 which exhibits the same local structural properties as captured by experimental NMR and the same electronic properties as captured by XAS.

By using first principles methods to generate a model of a-Al_2O_3, this enables the calculation of electronic properties, such as the eDOS, NMR and XAS, which is not possible using classical simulation methods. This is especially important for functional materials such as alumina, which are routinely used in electronic devices. We further demonstrate the importance of incorporating experimental insight at the model configuration sampling stage, as we describe a set of 54 different AIMD simulations, all with sensible initial conditions and RDFs, but only two of which had coordination environments within the experimental margin of error. This additionally underscores the need for having a specific experimental comparison metric when generating amorphous models; the results presented in this work are all with reference to one ALD deposited sample of alumina using the most relevant possible spectroscopy methods for characterization.

Given the capabilities of first principle methods used today, producing amorphous eDOS, and in turn NMR and XAS spectra as we have done in this work to understand the electronic structure of a-Al_2O_3, is certainly achievable for other amorphous systems. The method of averaging across static configurations from experimentally directed sampling of configurations from AIMD simulations can be applied to other amorphous systems and used to calculate electronic properties from first principles methods that are otherwise unattainable using large system sizes. We expect that given the transferability of this method, calculating these spectral properties, and potentially others will become the norm for simulations on amorphous solids, and especially in the field of device physics, encourage progress in fine tuning the electronic properties of these materials.

Author Contributions

AF Harper: Formal analysis, Writing - Original draft preparation, Data curation, Conceptualization. **SE Emge:** Investigation, Writing - review and editing. **PCMM Magusin:** Support with MQMAS setup and analysis, organization of 1 GHz measurements. **CP Grey:** Supervision, Resources, Writing - review and editing. **AJ Morris:** Supervision, Resources, Writing-review and editing.

Conflicts of interest

There are no conflicts to declare.

Acknowledgements

The authors thank Steve Haws (Henry Royce Institute, Cambridge) for assistance with the ALD and Richard Chen (University of Cambridge, Chemistry) for NMR sample preparation. The authors also thank Dr Trent Franks and the UK High-Field Solid-State NMR Facility Warwick for measurements on the 1 GHz magnet. **Funding:** AFH acknowledges the financial support of the Gates Cambridge Trust and the Winton Programme for the Physics of Sustainability, University of Cambridge, UK. AJM acknowledges funding from EPSRC (EP/P003532/1). The authors acknowledge networking support via the EPSRC Collaborative Computational Projects, CCP9 (EP/M022595/1) and CCP-NC (EP/T026642/1). This work was performed using resources provided by the Cambridge Service for Data Driven Discovery (CSD3) operated by the University of Cambridge Research Computing Service (www.csd3.cam.ac.uk), provided by Dell EMC and Intel using Tier-2 funding from the EPSRC (capital grant EP/P020259/1), and DiRAC funding from the Science and Technology Facilities Council (www.dirac.ac.uk). SPE acknowledges funding via an EPSRC iCASE (Award 1834544) and via the Royal Society (RP\R1\180147). For ALD sample preparation, use of the Ambient Processing Cluster Tool, part of Sir Henry Royce Institute - Cambridge Equipment, EPSRC grant EP/P024947/1 is gratefully acknowledged.

Notes and references

(1) Hoja, J.; Ko, H.-Y.; Neumann, M. A.; Car, R.; DiStasioJr., R. A.; Tkatchenko, A. Reliable and Practical Computational Description of Molecular Crystal Polymorphs. *Science Advances* **2019**, *45* (12). https://doi.org/10.1126/SCIADV.AAU3338.

(2) Woodley, S.; Catlow, R. Crystal Structure Prediction from First Principles. *Nat Mater* **2008**, *7* (12), 937–946. https://doi.org/10.1038/NMAT2321.

(3) Sivaraman, G.; Krishnamoorthy, A. N.; Baur, M.; Holm, C.; Stan, M.; Csányi, G.; Benmore, C.; Vázquez-Mayagoitia, Á. Machine-Learned Interatomic Potentials by Active Learning: Amorphous and Liquid Hafnium Dioxide. *npj Computational Materials 2020 6:1* **2020**, *6* (1), 1–8. https://doi.org/10.1038/s41524-020-00367-7.

(4) Deringer, V. L.; Bernstein, N.; Csányi, G.; ben Mahmoud, C.; Ceriotti, M.; Wilson, M.; Drabold, D. A.; Elliott, S. R. Origins of Structural and Electronic Transitions in Disordered Silicon. *Nature* **2021**, *589* (7840), 59–64. https://doi.org/10.1038/s41586-020-03072-z.

(5) Aykol, M.; Dwaraknath, S. S.; Sun, W.; Persson, K. A. Thermodynamic Limit for Synthesis of Metastable Inorganic Materials. *Science Advances* **2018**, *4* (4). https://doi.org/10.1126/SCIADV.AAQ0148.

(6) Das, C.; Kot, M.; Hellmann, T.; Wittich, C.; Mankel, E.; Zimmermann, I.; Schmeisser, D.; Khaja Nazeeruddin, M.; Jaegermann, W. Atomic Layer-Deposited Aluminum Oxide Hinders Iodide Migration and Stabilizes Perovskite Solar Cells. *Cell Reports Physical Science* **2020**, *1* (7), 100112. https://doi.org/10.1016/J.XCRP.2020.100112.

(7) Yang, Z.; Albrow-Owen, T.; Cui, H.; Alexander-Webber, J.; Gu, F.; Wang, X.; Wu, T. C.; Zhuge, M.; Williams, C.; Wang, P.; Zayats, A. v.; Cai, W.; Dai, L.; Hofmann, S.; Overend, M.; Tong, L.; Yang, Q.; Sun, Z.; Hasan, T. Single-Nanowire Spectrometers. *Science (1979)* **2019**, *365* (6457), 1017–1020. https://doi.org/10.1126/SCIENCE.AAX8814.

(8) Lu, J.; Fu, B.; Kung, M.; Xiao, G.; Elam, J.; Kung, H.; Stair, P. Coking- and Sintering-Resistant Palladium Catalysts Achieved through Atomic Layer Deposition. *Science* **2012**, *335* (6073), 1205–1208. https://doi.org/10.1126/SCIENCE.1212906.

(9) Fukuhara, M.; Kuroda, T.; Hasegawa, F.; Hashida, T.; Takeda, M.; Konno, K.; Fujima, N. AlO6 Clusters' Electric Storage Effect in Amorphous Alumina Supercapacitors. *Scientific Reports 2021 11:1* **2021**, *11* (1), 1–6. https://doi.org/10.1038/s41598-021-81483-2.

(10) Kim, M. G.; Kanatzidis, M. G.; Facchetti, A.; Marks, T. J. Low-Temperature Fabrication of High-Performance Metal Oxide Thin-Film Electronics via Combustion Processing. *Nature Materials 2011 10:5* **2011**, *10* (5), 382–388. https://doi.org/10.1038/nmat3011.

(11) Caro, M. A.; Aarva, A.; Deringer, V. L.; Csányi, G.; Laurila, T. Reactivity of Amorphous Carbon Surfaces: Rationalizing the Role of Structural Motifs in Functionalization Using Machine Learning. *Chemistry of Materials* **2018**, *30* (21), 7446–7455. https://doi.org/10.1021/ACS.CHEMMATER.8B03353/SUPPL_FILE/CM8B03353_SI_001.PDF.

(12) Deringer, V. L.; Csányi, G. Machine Learning Based Interatomic Potential for Amorphous Carbon. *Physical Review B* **2017**, *95* (9), 094203. https://doi.org/10.1103/PHYSREVB.95.094203/FIGURES/16/MEDIUM.

(13) Zhou, Y.; Kirkpatrick, W.; Deringer, V. L.; Zhou, Y.; Kirkpatrick, W.; Deringer, V. L. Cluster Fragments in Amorphous Phosphorus and Their Evolution under Pressure. *Advanced Materials* **2021**, 2107515. https://doi.org/10.1002/ADMA.202107515.

(14) Artrith, N.; Urban, A.; Ceder, G. Constructing First-Principles Phase Diagrams of Amorphous LixSi Using Ml Assisted Sampling. *The Journal of Chemical Physics* **2018**, *148*, 241711. https://doi.org/10.1063/1.5017661.

(15) Paruzzo, F. M.; Hofstetter, A.; Musil, F.; De, S.; Ceriotti, M.; Emsley, L. Chemical Shifts in Molecular Solids by Machine Learning. *Nature Communications 2018 9:1* **2018**, *9* (1), 1–10. https://doi.org/10.1038/s41467-018-06972-x.

(16) Torrisi, S. B.; Carbone, M. R.; Rohr, B. A.; Montoya, J. H.; Ha, Y.; Yano, J.; Suram, S. K.; Hung, L. Random Forest Machine Learning Models for Interpretable X-Ray Absorption near-Edge Structure Spectrum-Property Relationships. *npj Computational Materials 2020 6:1* **2020**, *6* (1), 1–11. https://doi.org/10.1038/s41524-020-00376-6.

(17) Puurunen, R. L. Surface Chemistry of Atomic Layer Deposition: A Case Study for the Trimethylaluminum/Water Process. *Journal of Applied Physics* **2005**, *97* (12), 121301. https://doi.org/10.1063/1.1940727.

(18) George, S. M. Atomic Layer Deposition: An Overview. *Chemical Reviews* **2009**, *110* (1), 111–131. https://doi.org/10.1021/CR900056B.

(19) Zhao, Y.; Amirmaleki, M.; Sun, Q.; Zhao, C.; Codirenzi, A.; Goncharova, L. v.; Wang, C.; Adair, K.; Li, X.; Yang, X.; Zhao, F.; Li, R.; Filleter, T.; Cai, M.; Sun, X. Natural SEI-Inspired Dual-Protective Layers via Atomic/Molecular Layer Deposition for Long-Life Metallic Lithium Anode. *Matter* **2019**, *1* (5), 1215–1231. https://doi.org/10.1016/J.MATT.2019.06.020.

(20) Lotfabad, E. M.; Kalisvaart, P.; Cui, K.; Kohandehghan, A.; Kupsta, M.; Olsen, B.; Mitlin, D. ALD TiO2 Coated Silicon Nanowires for Lithium Ion Battery Anodes with Enhanced Cycling Stability and Coulombic Efficiency. *Physical Chemistry Chemical Physics* **2013**, *15* (32), 13646–13657. https://doi.org/10.1039/C3CP52485J.

(21) Zhao, Y.; Goncharova, L. v.; Lushington, A.; Sun, Q.; Yadegari, H.; Wang, B.; Xiao, W.; Li, R.; Sun, X. Superior Stable and Long Life Sodium Metal Anodes Achieved by Atomic Layer Deposition. *Advanced Materials* **2017**, *29* (18), 1606663. https://doi.org/10.1002/ADMA.201606663.

(22) Chang, C.-Y.; Lee, K.-T.; Huang, W.-K.; Siao, H.-Y.; Chang, Y.-C. High-Performance, Air-Stable, Low-Temperature Processed Semitransparent Perovskite Solar Cells Enabled by Atomic Layer Deposition. *Chemistry of Materials* **2015**, *27* (14), 5122–5130. https://doi.org/10.1021/ACS.CHEMMATER.5B01933.

(23) Gao, Z.; Qin, Y. Design and Properties of Confined Nanocatalysts by Atomic Layer Deposition. *Accounts of Chemical Research* **2017**, *50* (9), 2309–2316. https://doi.org/10.1021/ACS.ACCOUNTS.7B00266.

(24) O'Neill, B. J.; Jackson, D. H. K.; Lee, J.; Canlas, C.; Stair, P. C.; Marshall, C. L.; Elam, J. W.; Kuech, T. F.; Dumesic, J. A.; Huber, G. W. Catalyst Design with Atomic Layer Deposition. *ACS Catalysis* **2015**, *5* (3), 1804–1825. https://doi.org/10.1021/CS501862H.

(25) Chan, J. C. C.; Eckert, H. High-Resolution 27Al-19F Solid-State Double Resonance NMR Studies of AlF3-BaF2-CaF2 Glasses. *Journal of Non-Crystalline Solids* **2001**, *284* (1–3), 16–21. https://doi.org/10.1016/S0022-3093(01)00373-8.

(26) Massiot, D.; Fayon, F.; Capron, M.; King, I.; St´, S.; le Calvé, S.; Calvé, C.; Alonso, B.; Durand, J.-O.; Bujoli, B.; Gan, Z.; Hoatson, G. Modelling One-and Two-Dimensional Solid-State NMR Spectra. *Magn. Reson. Chem* **2002**, *40*, 70–76. https://doi.org/10.1002/mrc.984.

(27) Engelhardt, G.; Koller, H. A Simple Procedure for the Determination of the Quadrupole Interaction Parameters and Isotropic Chemical Shifts from Magic Angle Spinning NMR Spectra of Half-Integer Spin Nuclei in Solids. *Magnetic Resonance in Chemistry* **1991**, *29* (9), 941–945. https://doi.org/10.1002/MRC.1260290914.

(28) Kresse, G.; Furthmüller, J. Efficient Iterative Schemes for *Ab Initio* Total-Energy Calculations Using a Plane-Wave Basis Set. *Physical Review B* **1996**, *54* (16), 11169. https://doi.org/10.1103/PhysRevB.54.11169.

(29) Evans, D. J.; Holian, B. L. The Nose–Hoover Thermostat. *The Journal of Chemical Physics* **1998**, *83* (8), 4069. https://doi.org/10.1063/1.449071.

(30) Blöchl, P. E. Projector Augmented-Wave Method. *Physical Review B* **1994**, *50* (24), 17953. https://doi.org/10.1103/PhysRevB.50.17953.

(31) Clark, S. J.; Segall, M. D.; Pickard, C. J.; Hasnip, P. J.; Probert, M. I. J.; Refson, K.; Payne, M. C. First Principles Methods Using CASTEP. *Zeitschrift für Kristallographie - Crystalline Materials* **2005**, *220* (5–6), 567–570. https://doi.org/10.1524/ZKRI.220.5.567.65075.

(32) Pickard, C. J.; Mauri, F. All-Electron Magnetic Response with Pseudopotentials: NMR Chemical Shifts. *Physical Review B* **2001**, *63* (24), 245101. https://doi.org/10.1103/PhysRevB.63.245101.

(33) Bak, M.; Rasmussen. JT; Nielsen, N. SIMPSON: A General Simulation Program for Solid-State NMR Spectroscopy. *J Magn Reson* **2000**, *147* (2), 296–330. https://doi.org/10.1006/JMRE.2000.2179.

(34) Gao, S.-P.; Pickard, C. J.; Perlov, A.; Milman, V. Core-Level Spectroscopy Calculation and the Plane Wave Pseudopotential Method. *Journal of Physics: Condensed Matter* **2009**, *21* (10), 104203. https://doi.org/10.1088/0953-8984/21/10/104203.

(35) Clark, S. J.; Segall, M. D.; Pickard, C. J.; Hasnip, P. J.; Probert, M. I. J.; Refson, K.; Payne, M. C. First Principles Methods Using {CASTEP}. *Zeitschrift für Kristallographie - Crystalline Materials* **2005**, *220* (5/6), 567 – 570. https://doi.org/10.1524/zkri.220.5.567.65075.

(36) Nicholls, R. J.; Morris, A. J.; Pickard, C. J.; Yates, J. R. OptaDOS - a New Tool for EELS Calculations. *Journal of Physics: Conference Series* **2012**, *371* (1), 012062. https://doi.org/10.1088/1742-6596/371/1/012062.

(37) Morris, A. J.; Nicholls, R. J.; Pickard, C. J.; Yates, J. R. OptaDOS: A Tool for Obtaining Density of States, Core-Level and Optical Spectra from Electronic Structure Codes. *Computer Physics Communications* **2014**, *185* (5), 1477–1485. https://doi.org/10.1016/J.CPC.2014.02.013.

(38) Yates, J. R.; Wang, X.; Vanderbilt, D.; Souza, I. Spectral and Fermi Surface Properties from Wannier Interpolation. *Physical Review B* **2007**, *75* (19), 195121. https://doi.org/10.1103/PhysRevB.75.195121.

(39) Mizoguchi, T.; Tanaka, I.; Gao, S.-P.; Pickard, C. J. First-Principles Calculation of Spectral Features, Chemical Shift and Absolute Threshold of ELNES and XANES Using a Plane Wave Pseudopotential Method. *Journal of Physics: Condensed Matter* **2009**, *21* (10), 104204. https://doi.org/10.1088/0953-8984/21/10/104204.

(40) Liu, D.; Guo, Y.; Lin, L.; Robertson, J. First-Principles Calculations of the Electronic Structure and Defects of Al2O3. *Journal of Applied Physics* **2013**, *114* (8), 083704. https://doi.org/10.1063/1.4818475.

(41) Momida, H.; Hamada, T.; Takagi, Y.; Yamamoto, T.; Uda, T.; Ohno, T. Theoretical Study on Dielectric Response of Amorphous Alumina. *Physical Review B - Condensed Matter and Materials Physics* **2006**, *73* (5), 054108. https://doi.org/10.1103/PHYSREVB.73.054108/FIGURES/9/MEDIUM.

(42) Lizárraga, R.; Holmström, E.; Parker, S. C.; Arrouvel, C. Structural Characterization of Amorphous Alumina and Its Polymorphs from First-Principles XPS and NMR Calculations. *PHYSICAL REVIEW B* **2011**, *83*, 94201. https://doi.org/10.1103/PhysRevB.83.094201.

(43) Sarou-Kanian, V.; Gleizes, A. N.; Florian, P.; Samélor, D.; Massiot, D.; Vahlas, C. Temperature-Dependent 4-, 5- and 6-Fold Coordination of Aluminum in MOCVD-Grown Amorphous Alumina Films: A Very High Field 27Al-NMR Study. *Journal of Physical Chemistry C* **2013**, *117* (42), 21965–21971.

https://doi.org/10.1021/JP4077504/SUPPL_FILE/JP4077504_SI_001.PDF.

(44) Lee, S. M.; Cahill, D. G.; Allen, T. H. Thermal Conductivity of Sputtered Oxide Films. *Physical Review B* **1995**, *52* (1), 253. https://doi.org/10.1103/PhysRevB.52.253.

(45) Lizárraga, R.; Holmström, E.; Parker, S. C.; Arrouvel, C. Structural Characterization of Amorphous Alumina and Its Polymorphs from First-Principles XPS and NMR Calculations. *Physical Review B* **2011**, *83*, 94201. https://doi.org/10.1103/PhysRevB.83.094201.

(46) Aykol, M.; Persson, K. A. Oxidation Protection with Amorphous Surface Oxides: Thermodynamic Insights from Ab Initio Simulations on Aluminum. **2018**. https://doi.org/10.1021/acsami.7b14868.

(47) Martínez, L.; Andrade, R.; Birgin, E. G.; Martínez, J. M. PACKMOL: A Package for Building Initial Configurations for Molecular Dynamics Simulations. *Journal of Computational Chemistry* **2009**, *30* (13), 2157–2164. https://doi.org/10.1002/JCC.21224.

(48) Lamparter, P.; Kniep, R. Structure of Amorphous Al2O3. *Physica B: Condensed Matter* **1997**, *234–236*, 405–406. https://doi.org/10.1016/S0921-4526(96)01044-7.

(49) Lee, S. K.; Park, S. Y.; Yi, Y. S.; Moon, J. Structure and Disorder in Amorphous Alumina Thin Films: Insights from High-Resolution Solid-State NMR. *Journal of Physical Chemistry C* **2010**, *114* (32), 13890–13894. https://doi.org/10.1021/JP105306R.

(50) Kaushik, M.; Leroy, C.; Chen, Z.; Gajan, D.; Willinger, E.; Mü Ller, C. R.; Fayon, F.; Massiot, D.; Fedorov, A.; Copéret, C.; Lesage, A.; Florian, P. Atomic-Scale Structure and Its Impact on Chemical Properties of Aluminum Oxide Layers Prepared by Atomic Layer Deposition on Silica. *Cite This: Chem. Mater* **2021**, *33*, 3348. https://doi.org/10.1021/acs.chemmater.1c00516.

(51) Waroquiers, D.; Gonze, X.; Rignanese, G.-M.; Welker-Nieuwoudt, C.; Rosowski, F.; Göbel, M.; Schenk, S.; Degelmann, P.; André, R.; Glaum, R.; Hautier, G. Statistical Analysis of Coordination Environments in Oxides. *Chemistry of Materials* **2017**, *29* (19), 8346–8360. https://doi.org/10.1021/ACS.CHEMMATER.7B02766.

(52) Neuville, D. R.; Cormier, L.; Massiot, D. Al Environment in Tectosilicate and Peraluminous Glasses: A 27Al MQ-MAS NMR, Raman, and XANES Investigation. *Geochimica et Cosmochimica Acta* **2004**, *68* (24), 5071–5079. https://doi.org/10.1016/J.GCA.2004.05.048.

(53) Cabaret, D.; Brouder, C. Origin of the Pre-Edge Structure at the Al K-Edge: The Role of Atomic Vibrations. *Journal of Physics: Conference Series* **2009**, *190* (1), 012003. https://doi.org/10.1088/1742-6596/190/1/012003.

(54) Filatova, E. O.; Konashuk, A. S. Interpretation of the Changing the Band Gap of Al2O3 Depending on Its Crystalline Form: Connection with Different Local Symmetries. *Journal of Physical Chemistry C* **2015**, *119* (35), 20755–20761. https://doi.org/10.1021/ACS.JPCC.5B06843/ASSET/IMAGES/LARGE/JP-2015-06843N_0002.JPEG.

(55) Podder, J.; Lin, J.; Sun, W.; Botis, S. M.; Tse, J.; Chen, N.; Hu, Y.; Li, D.; Seaman, J.; Pan, Y. Iodate in Calcite and Vaterite: Insights from Synchrotron X-Ray Absorption Spectroscopy and First-Principles Calculations. *Geochimica et Cosmochimica Acta* **2017**, *198*, 218–228. https://doi.org/10.1016/J.GCA.2016.11.032.

(56) Mao, Y.; Liang, X. X.; Zhao, G. J.; Song, T. L. The Structural and Optical Properties of Ternary Mixed Crystals InxGa1−xAs with Zinc-Blende Structure by First-Principle Calculations. *Physica B: Condensed Matter* **2019**, *569*, 87–95. https://doi.org/10.1016/J.PHYSB.2019.05.042.

(57) Bugnet, M.; Jaouen, M.; Mauchamp, V.; Cabioc'H, T.; Hug, G. Experimental and First-Principles Investigation of the Electronic Structure Anisotropy of Cr2AlC. *Physical Review B - Condensed Matter and Materials Physics* **2014**, *90* (19), 195116. https://doi.org/10.1103/PHYSREVB.90.195116/FIGURES/21/MEDIUM.

(58) Shen, Y.; Yang, X.; Bian, Y.; Liu, S.; Tang, K.; Zhang, R.; Zheng, Y.; Gu, S. First Principles Study on the Structural Stability and Optoelectronic Properties of InxGa1−xAs Materials with Different Indium Component. *Materials Research Express* **2018**, *5* (1), 015912. https://doi.org/10.1088/2053-1591/AAA7A8.

(59) VL, D.; N, B.; AP, B.; MJ, C.; RN, K.; LE, M.; CP, G.; SR, E.; G, C. Realistic Atomistic Structure of Amorphous Silicon from Machine-Learning-Driven Molecular Dynamics. *J Phys Chem Lett* **2018**, *9* (11), 2879–2885. https://doi.org/10.1021/ACS.JPCLETT.8B00902.

(60) Mais, M.; Paul, S.; Barrow, N. S.; Titman, J. J. Dynamic Nuclear Polarisation Enhanced Solid-State Nuclear Magnetic Resonance Studies of Surface Modification of ?-Alumina. *Johnson Matthey Technology Review* **2018**, *62* (3), 271–278. https://doi.org/10.1595/205651318X696765.